Examining and Optimising Far-Field Multi-Probe Anechoic Chambers for 5GNR OTA Testing of Massive MIMO Systems

S.F. Gregson[1,2], C.G. Parini[2]
[1] Next Phase Measurements, Garden Grove, USA, stuart.gregson@npmeas.com
[2] Queen Mary University of London, London, UK

***Abstract*— Direct far-field (DFF) testing has become the de facto standard for sub-6 GHz over the air (OTA) testing of the physical layer of radio access networks with the far-field multi-probe anechoic chamber (FF-MPAC) being especially widely deployed for the verification of massive multiple input multiple output (Massive MIMO) antennas in the presence of several users. The adoption of mm-wave bands within the fifth generation new radio (5G NR) specification has meant that, as these systems require the user equipment be placed in the far-field of the base transceiver station (BTS) antenna, either excessively large FF-MPAC test systems are required or, the user equipment is paced at range-lengths very much shorter than that suggested by the classical Rayleigh criteria. This paper explores range length effects on several communication system figures of merit and examines the consequences of testing within smaller enclosures. Results are presented and discussed.**

***Index Terms*—Far-Field Multi-Probe Anechoic Chamber, FF-MPAC, 5G NR, Massive-MIMO, OTA, EVM.**

I. INTRODUCTION

The launch of 5G New Radio (5G NR) ushers in a completely new air interface to underpin the next generation of mobile telecommunication systems. 5G NR promises a significant increase in data throughput requiring the adoption of several new technologies in the RF system that encompasses both the mobile user equipment (UE) and the base transceiver station (BTS) [1, 2]. Although the frequency band below 6 GHz may be used during the initial deployment stage, 5G technologies will mainly operate in the 28 GHz frequency band, or higher, requiring the widespread deployment of more complex, electrically larger, massive MIMO (Multiple Input Multiple Output) active antenna architectures [1, 2] within the BTS system.

The test and measurement market have, to a large extent, attempted to respond to this new requirement by adapting and redeploying traditional sub-6 GHz test and measurement methodologies in the mm-wave band. The far-field multi-probe anechoic chamber (FF-MPAC) is an example of a traditional approach that has been particularly widely deployed for the sub-6 GHz testing of massive multiple input multiple output (Massive MIMO) antennas [3], that is now being repurposed for the corresponding mm-wave application. However, when using the direct far-field (DFF) method, the antenna under test (AUT) is typically considered to be separated from the remote source antenna by a distance that is proportional to the frequency and proportional to the square of the maximum dimension of the AUT [4]. Unfortunately, this suggests that when using the direct far-field (DFF) method at mm-wave frequencies, for all but the electrically smallest of BTS antennas, indoor screened test systems become impractically large and therefore uneconomic. However in the context of OTA testing, traditional far-field (FF) antenna parameters have become far less significant than was previously the case, with instead, focus largely shifting toward communication system parameters such as far-field error vector magnitude (EVM), bit error rate (BER), and of course, absolute data throughput [5, 6]. Thus, as the design, configuration and cost of a FF-MPAC is primarily predicated upon the range length used, it is crucial that we carefully and quantitatively examine the impact that changes in range length have on the communication system primary figures of merit, in the knowledge of the amount of error that a given test application can tolerate.

The characteristics of the electromagnetic (EM) fields that are set-up by the accelerating charges present within the radiating antenna vary with distance [4]. And, although the characteristics of these fields vary continuously with distance, it has proved useful for engineers to identify distinct zones in which to characterise the general properties of the fields while accepting that no hard boundaries exist between these regions and that the exact boundaries themselves are not defined precisely. As the distance from the radiator is increased there eventually becomes a point where the angular radiation pattern becomes largely independent of the distance, with the longitudinal components of the EM field becoming negligible, and the electric and magnetic fields being related by the impedance of free space. This far-field zone, or Fraunhofer zone as it is also called is named due to its analog with the optical case. This distance varies from one type of antenna to another. However, for electrically large antennas radiating in free space which have a well-defined coherent radiating aperture, a commonly used criteria which formalises the relationship with electrical size stated above is [4],

$$R_{FF} = 2D^2 f / c \quad (1)$$

This is known as Rayleigh's far-field criteria in which D denotes the largest dimension of the aperture, f is the frequency and c is the speed of light in a vacuum. If an aperture antenna, *e.g.* a Massive MIMO antenna, is measured at this distance, with the antenna being ideally situated about the origin of the measurement coordinate system, then the measured patterns do not deviate appreciably from the value that would be measured were instead the antenna to be placed at an infinite distance. Although this is a widely used criteria, others exist since non-aperture type antennas behave in a different way [7] with varying degrees of tolerance to experimental error resulting in the requirement for further, smaller or larger, test distances [7, 8] with for example the space sector often using twice the distance suggested by (1) on the basis of conservatism.

In this paper we investigate the sensitivity of various figures of merit including equivalent isotropic radiated power (EIRP), error vector magnitude (EVM), symbol error rate as well as the classical antenna pattern to the amplitude and phase curvature imposed across the AUT at a variety of range lengths for the example of a mm-wave Massive MIMO antenna. The next section introduced the FF-MPAC in more detail with subsequent sections examining the impact of the variation in range length on measurement.

II. Overview of the FF-MPAC

Of the available Massive MIMO OTA test methods, the FF-MPAC has becomes one of the most attractive methods for reproducing a realistic multipath rich wireless channel environment. Figure 1 below presents a schematic representation of a typical sectorized FF-MPAC [3]. This system comprises a screened anechoic chamber into which the device under test (DUT) is placed. The chamber also contains an array of, typically fixed, OTA probes which can number *circa* 100 individual probes that, when distributed over a spherical sector can be used to cover a range of possible azimuth and elevation angles as seen by the DUT, which in this case is the Massive MIMO BTS antenna.

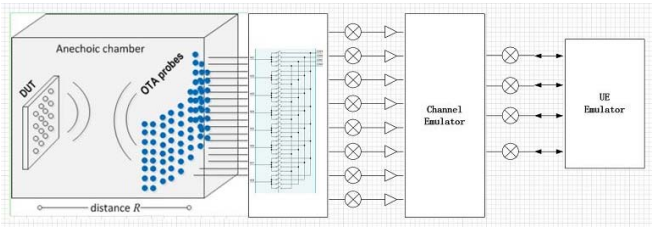

Fig. 1. Example of a typical sectorized FF-MPAC chamber.

Here the individual, dual (nominally horizontally and vertically) polarized OTA probes are connected via a switching matrix which comprises assorted RF switches, filters and amplifiers that are required to channel and condition the signal to and from the channel emulator. The signal link is then mixed down from the mm-wave frequency of the AUT to the sub-6 GHz frequency required by the channel and UE emulators. The channel emulator adds fading test scenarios to the signal whereupon it is detected/transmitted and measured via the UE emulator which can handle, typically, four input/output links. This test system is typically used in one of two modes. In the first scenario, only a simple model is used to recreate a given environment without any multipath effects and therefore one probe per link is used within the OTA test chamber. Some fading can be added to the signal link to simulate the effects of, for example, dispersion, Doppler. However, this model is limited and does not generally represent the rich scattering environment that would be encountered in practice. Alternatively, this system can be used to test within a multipath and clustering rich environment. In this scenario several probes are used per link to simulate the effects of multipath and different angles of arrival. The probes chosen are separated by a distance that is sufficiently large to prevent their behaving as a single source whilst also ensuring that each probe-cluster is illuminated by only a single AUT beam. This model is more representative of the scattering environment that the AUT will eventually be required to operate within.

The next section presents results of a series of simulations of a FF-MPAC test system designed to illuminate an array AUT between 24 GHz to 39 GHz with the aim of investigating the sensitivity of EVM, symbol error rate and antenna pattern to amplitude and phase curvature across the AUT at a range of different range lengths and antenna states.

III. Simulated Measurement of AUT in FF-MPAC

Here, as in our previous studies, *e.g.* [6], we have simulated the Massive MIMO AUT as an array of infinitesimal half wave dipoles each orientated at 45° to the horizontal with the array elements spaced half wavelength apart (at 26 GHz) on a rectangular lattice yielding a diagonal dimension of 206 mm. Thus, the Fraunhofer distance at 24 GHz is 6.8 m; at 26 GHz is 7.4 m and at 39 GHz is 11.0 m with the centre frequency being used in this work. For the purposes of simulation of the OTA measurement process of the FF-MPAC probe antenna was fixed at the desired distance at 26 GHz and the AUT was physically rotated to determine the "measured" radiation pattern. This was implemented by evaluating the mutual impedance, Z_{21}, using a formula based upon a reciprocity relation [4, 6],

$$Z_{21} = -\frac{1}{I_{11} I_{22}} \int_{S_2} \left(\underline{E}_2 \times \underline{H}_1 - \underline{E}_1 \times \underline{H}_2 \right) \cdot \hat{\underline{n}} \, ds \quad (2)$$

Thus, we see that the quality of our measurement depends to a large extent on how well the electric and magnetic fields $\underline{E}_2$ & $\underline{H}_2$ respectively approximate a perfect TEM plane-wave across the AUT which is represented by the fields $\underline{E}_1$ & $\underline{H}_1$. In this study, the OTA probe was taken to be a cylindrically symmetrical corrugated horn with a pattern that dropped off by 3.6 dB at 20° from boresight. To determine the performance when the array is electronically scanned, we first steer the beam to the desired direction and then, again, physically rotate the AUT to determine the

"measured" radiation pattern. To cover the desired range of scan, we have determined the systems performance as a function of distance for the cases of boresight beam, 30° azimuth scanned beam, and a 60° azimuth scanned beam.

Figure 2 shows the simulated "measured" radiation pattern of the array when illuminated by the probe at a range of FF distances of 1/10 R_{FF}, 1/4 R_{FF}, 1/3 R_{FF}, ½ R_{FF}, R_{FF}, 2 R_{FF}. When the range length is equal to the far-field distance, the phase curvature across the aperture of the antenna is, by our definition, π/8 rad = 22.5°. This means that at twice the far-field distance as estimated by (1), the phase curvature will be 11.25° (*cf.* this is approximately equal to the CATR quiet-zone phase ripple specification [4]). Similarly, at half the FF distance the phase curvature will increase to 45°, and will vary proportionally for the other distances. Here, to illustrate the loss in received power as a function of distance we have normalized the results at 0 dB for the case of boresight at 2×R_{FF}. At 26 GHz the FF distance for the array is R_{FF} = 7.4 m and, it is clear that, apart from the 1/10 R_{FF} case the shape of the AUT pattern can be clearly determined. Closer examination reveals that the antenna pattern main beam exhibits a reduction in gain (compared to the x2 R_{FF} case) of 0.12 dB and 0.25 dB respectively for the ½ R_{FF} case and 1/3 R_{FF} distances.

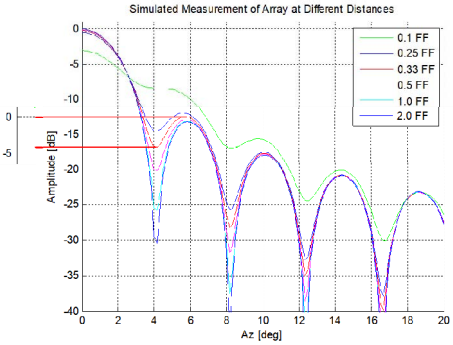

Fig. 2. AUT radiation pattern at 26 GHz illuminated by probe at different R_{FF} distances. 1.0 R_{FF} = 7.4 m. For comparison the change in power due to the $1/r^2$ term has been supressed.

Examining the near-in side-lobes for all the range distances shows that apart from the 1/10 R_{FF} case all show the location of the side-lobe peak and null positions to good accuracy. However, the null depth for the 1/4 R_{FF} case is very small for the first side-lobe (less than 3 dB) and so this is poorly defined. For MIMO applications, null location and depth are important parameters thus the 1/3 R_{FF} and ½ R_{FF} cases clearly offer a good "measured" pattern performance at reduced range lengths. For the 1/3 R_{FF} case the null depth is shown to be *circa* 4 dB in Figure 2.

To examine at the EVM performance we have followed the same procedure as in our previous studies [6, 9] and have calculated the S_{21} transmission coefficient results at 26 GHz over a 400 MHz bandwidth for several mechanical azimuth rotations of the AUT with respect to the incoming quiet-zone (QZ) field. Figures 3 – 8 present S_{21} plotted over the 400 MHz 5G band for different far-field distances with the antenna boresight pointing to range of azimuth angles from 0° to 40°. The significant variation in S_{21} with frequency at 30° azimuth reflects the fact that the side-lobe region (and null at 30°) of the AUT will change rapidly with frequency.

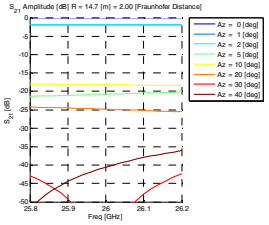

Fig. 3. S_{21} plotted at 2 R_{FF}.

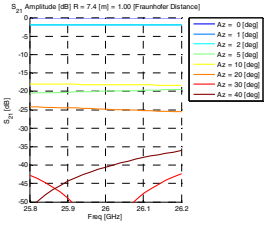

Fig. 4. S_{21} plotted at R_{FF}.

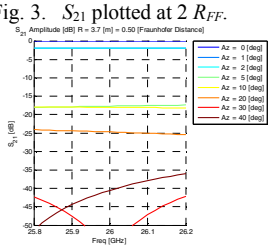

Fig. 5. S_{21} plotted at ½ R_{FF}.

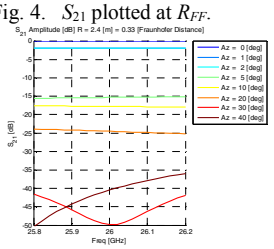

Fig. 6. S_{21} plotted at 1/3 R_{FF}.

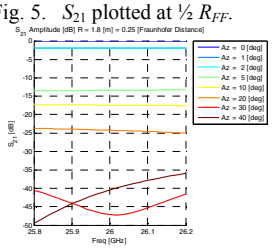

Fig. 7. S_{21} plotted at 1/4 R_{FF}.

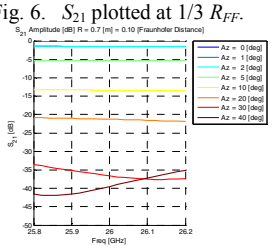

Fig. 8. S_{21} plotted at 1/10 R_{FF}.

Table 1 summarises the EVM and symbol error rate performance, ringed in red, at 30° azimuth (near the pattern null), and we see the change in EVM as the null is filled in with the decreasing range length. The definitions of EVM, symbol error rate and structural similarity index used in the preparation of Table 1 are defined in accordance with the open literature [6, 9]. Although these results were computed for all angles, due to the limitations of available space herein, only the important, more pathological, 30° case is presented. Clearly, from inspection of Table I, we may see that EVM is sensitive to the change in the pattern null, with symbol error rate less so, with a distance = 1/3 R_{FF} providing a reasonable compromise between distance and reliability of reported figure of merit (FoM). In cases such as this, the linear equalisation that is employed to reconstruct the constellation diagram and decode the complex quadrature amplitude modulated (QAM) signal become unreliable with the EVM values obtained increase accordingly [6, 9]. This is what we are seeing here with the resilience shown by the symbol error rate providing an illustration of one of the motivators for adopting digitally based communication technologies.

TABLE I. EVM CALCULATED WITH AUT ROTATED TO 30° (NEAR PATTERN NULL) FOR DIFFERENT RANGE DISTANCES (0° AUT BEAM SCAN ANGLE)

Range length (FF)	2	1	0.5	0.33	0.25	0.1
Range length (m)	14.722	7.361	3.6805	2.4291	1.8402	0.7361
Theta (deg)	30	30	30	30	30	30
Error Vector Magnitude (RMS)	65.90%	61.20%	52.00%	43.10%	36.20%	13.60%
Symbol Error Rate	87.30%	86.40%	85.20%	83.70%	81.70%	55.90%
Structural Similarity Index	0.3	0.4	0.4	0.5	0.6	0.8

We now repeat the analysis presented above with the array AUT beam scanned to 30° azimuth by applying a linear phase taper across the array elements to consider the case where the UE is not broadside to the array. Applying a linear phase taper to steer the beam of an array causes the pattern to shift linearly in direction cosine space (which corresponds to a non-linear translation in angle space), and results in a broadening of the main beam with a related scan loss which is determined by the embedded element pattern [10]. In general, mutual coupling within the finite array will also influence the pattern and this will change as the array is scanned. However, in this study as the elements were not extremely closely packed, these effects were ignored.

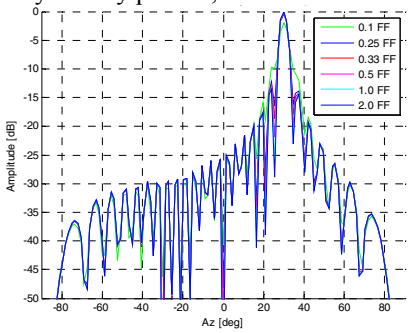

Fig. 9. AUT radiation pattern at 26 GHz with the beam electronically scanned by 30° illuminated by probe at different R_{FF} distances. 1.0 R_{FF} = 7.4 m.

When the main beam of the array was scanned to 30° in azimuth the main beam again showed gain reductions (when compared to the ×2 R_{FF} case) of 0.09 dB and 0.20 dB for the ½ R_{FF} case and 1/3 R_{FF} cases respectively. This is illustrated in Figure 9 where for comparison, the change in power due to the r^{-2} term has again been supressed. These gain reductions are a little less than the un-scanned equivalent cases. Similarly, the amount of side-lobe null filling is much less for a given FF distance than was observed in the boresight case. The reason for this is that as the AUT is physically rotated, the dimension of the antenna as "seen" by probe antenna becomes smaller, shown in green in Figure 10 below, and so the AUT incurs less phase distortion at a given range length relative to the boresight case.

Fig. 10. Illustration of AUT rotated to 30° with the beam electronically scanned back by 30° to be directed towards the UE, *i.e.* probe antenna.

Table II summarises the EVM and symbol error rate performance, for the case of Figure 9, at 0° azimuth (near pattern null), and we see the change in EVM as the null is filled in with the decreasing range length, *cf.* Table I for the physically rotated to 30° boresight scanned case for comparison, with the ¼ R_{FF} scanned case being similar to the 1/3 R_{FF} boresight case, again illustrating this effect of the reduced dimension of the array seen by the probe and its corresponding reduced phase taper across the array.

TABLE II. EVM CALCULATED WITH AUT ROTATED TO 0° (NEAR PATTERN NULL) FOR DIFFERENT RANGE DISTANCES (30° AUT BEAM SCAN ANGLE)

Range length (FF)	2	1	0.5	0.33	0.25	0.1
Range length (m)	14.722	7.361	3.6805	2.4291	1.8402	0.7361
Theta (deg)	0	0	0	0	0	0
Error Vector Magnitude (RMS)	67.70%	64.30%	57.70%	50.60%	44.70%	19.80%
Symbol Error Rate	87.40%	86.80%	86.40%	85.20%	83.80%	67.60%
Structural Similarity Index	0.3	0.3	0.4	0.5	0.5	0.8

The narrative around Figures 9 and 10 suggests that we may use a smaller FF distance as we scan out in azimuth based on looking at the azimuth pattern cuts. However, we need to realise that for the elevation cuts of the main beam at these scan angles, the "size" of the array as seen by the OTA feed in the elevation plane does *not* reduce and retains the same dimension as at boresight, *i.e.* the physical size of the array. Figure 11 shows the "measured" elevation pattern of the main beam for the case of the array beam scanned to 0° azimuth where again the change in power due to the r^{-2} term has been supressed.

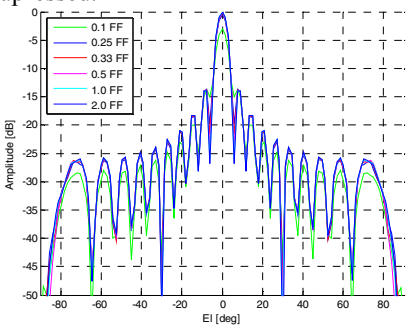

Fig. 11. Elevation pattern with array AUT beam steered to 0° in azimuth. Frequency 26 GHz illuminated by probe at different FF distances. 1.0 R_{FF} = 7.4 m.

Table III compares of first side-lobe null depth in both azimuth and elevation main beam patterns for both boresight and beam scanned to 30° in azimuth. Also shown is main beam gain loss for both beam scan cases. It is clear from this table that, as we scan the beam in azimuth, the azimuth pattern first side-lobe null depth improves for a given FF distance. However, for the corresponding elevation pattern this effect is *not* seen, confirming this to be due to the "size" of the array seen in the elevation scan plan remaining constant as the beam scans in azimuth.

TABLE III. COMPARISON OF FIRST SIDE-LOBE NULL DEPTH IN BOTH AZIMUTH AND ELEVATION PATTERNS AT BOTH BORESIGHT AND BEAM SCAN TO 30° IN AZIMUTH. ALSO SHOWN IS MAIN BEAM GAIN LOSS FOR BOTH BEAM SCAN CASES

beam scan	FF distance	sidelobe null depth, Az cut dB	sidelobe null depth, El cut dB	main beam gain loss
0 deg azimuth	0.5	7.0	9.5	0.12
0 deg azimuth	0.33	4.0	7.5	0.25
0 deg azimuth	0.25	2.5	6.0	0.5
30 deg azimuth	0.5	9.0	10.0	0.09
30 deg azimuth	0.33	6.0	7.5	0.2
30 deg azimuth	0.25	4.0	6.0	0.3

IV. CHAMBER SIZING

There is thus only limited scope to employ this effect and to the left-hand side of Figure 12 we propose a variable FF chamber concept where we see that between ±30° azimuth beam scans the FF distance is ½ R_{FF} giving excellent pattern

performance in both azimuth an elevation, dropping to 1/3 R_{FF} at 60° (Table IV) which gives excellent azimuth pattern performance and acceptable elevation pattern performance with the requirement here being to scan out to ±60° in azimuth and to the lesser amount of ±15° in elevation. Here, a chamber height of 2.8 m is needed for elevation scans of ±15° at ½ R_{FF}. Also shown to the right-hand side of Figure 12 is a size comparison of conventional FF chamber. The maximum frequency is 39 GHz.

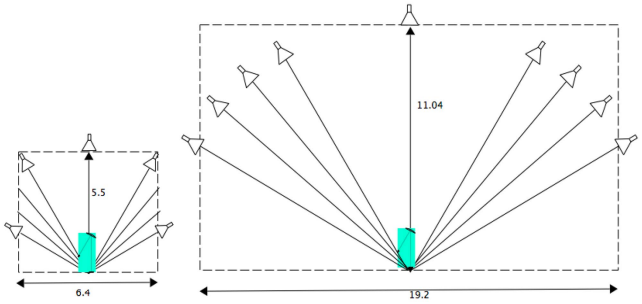

Fig. 12. Variable FF distance chamber design for FF-MPAC compared with traditional FF-MPAC.

TABLE IV. EFFECTIVE FF DISTANCE FOR AZIMUTH SCAN ANGLES FOR THE VARIABLE FF DISTANCE CHAMBER DESIGN FOR FF-MPAC.

Azimuth scan angle, [°]	Effective FF distance
0	0.50
30	0.50
40	0.44
50	0.37
60	0.33

Also shown in Fig 12 is a scale drawing of a single offset compact antenna test range (CATR) [4, 6] (highlighted by a cyan rectangle) that can measure the FF of the AUT array, but of course without the multibeam facility required of this FF-MPAC. Thus, although the optimised, reduced size, FF-MPAC is still noticeably larger that the single offset reflector CATR, it is considerably smaller than the baseline, conventional FF-MPAC test system. This offers a very considerable saving in the cost of the screened anechoic chamber, host building *etc.* as well as easing the spherical loss-factor in the RF link budget experienced at high frequencies. The trade-off is a marginal relaxation of the uncertainty in the antenna parameters but a negligible change in the communications systems primary figures of merit.

V. SUMMARY AND CONCLUSIONS

We have shown that we can successfully operate a FF-MPAC at a reduced FF range to provide a more compact, economical solution. A 1/3 R_{FF} at 39 GHz solution with range dimensions of (3.67 x 6.4 x 1.9) m can offer acceptable performance. Improved performance in the ±30° scan region can be achieved by increasing the size to (5.5 x 6.4 x2.8) m.

Inspection of Tables I and II shows that even in the demanding null-region, the symbol error rate changes by a percentage point for the ½ R_{FF} case when compared to the reference case, and just over one point for the even more extreme 1/3 R_{FF} case. Here, it is valuable to note that different modulation schemes require different EVMs. Thus, by assuming 256 QAM we have chosen a demanding case with EMV of better than *circa* 5% being typical of what would be needed in practice. However, by switching to lower order modulation schemes greater resilience may be achieved. As an example, for 64 QAM the EVM can vary from 2% to 12%. However, if we instead change to QPSK or 16 QAM, the required EVM can be increased further, *cf.* [11], illustrating the conservative nature of the treatment presented herein.

The worst-case assessment can be considered to be that of transmission of a high definition image. If the image can be recovered cleanly, then all other sources of error are acceptable. As measured by the anti-reductionist quantitative structural similarity index [6, 9, 12], we have shown that the reduction in range length has not impacted appreciably on the perceived image quality. Furthermore, the reduction in size of the variable FF distance chamber results presented here, offers a very considerable space saving of a factor of approximately 1/6 providing a significant cost saving in terms of real estate, chamber, absorber and so forth.

REFERENCES

[1] Wonil Roh, "5G Mobile Communications for 2020 and Beyond - Vision and Key Enabling Technologies," IEEE WCNC 2014 Keynote, Apr. 2014.

[2] Z. Pi and F. Khan, "An introduction to millimeter-wave mobile broadband systems," IEEE Commun. Mag., vol. 49, no. 6, pp. 101–107, Jun. 2011.

[3] M. Gustafsson, T. Jämsä, M. Högberg, "OTA Methods for 5G BTS Testing – Survey of Potential Approaches", 32nd URSI GASS, Montreal, 19-26 August 2017.

[4] C.G. Parini, S.F. Gregson, J. McCormick, D. Janse van Rensburg, "Theory and Practice of Modern Antenna Range Measurements", IET Press, 2014, ISBN 978-1-84919-560-7.

[5] *NR; Study on test methods, 3GPP TR 38.810: Release 16*, Table 5.3-2, Page 29, March 2019.

[6] S.F. Gregson, C.G. Parini, "Use of OTA System Performance Metrics in the Design & Optimization of CATRs for 5G Testing", AMTA Annual Symposium & Meeting, October 2019, San Diego, USA.

[7] A.W. Rudge, KJ. Milne, A.D. Olver, P. Knight, "The Handbook of Antenna Design Volume I", IEE EM Waves Series 15, Peter Perinus Ltd., 1982, ISBN 0-906048-82-6.

[8] C. Capps, "Near Field or Far Field?", EDN Mag, August, 2001.

[9] S.F. Gregson, C.G. Parini, "Compact Antenna Test Ranges: The Use of Simulation and Post-Processing Techniques in Support of 5G OTA Testing", 13th EuCAP, Invited Plenary Talk, 31st March to 5th April 2019, Krakaw, Poland.

[10] D. Kitchener, K. Raghavan, C.G. Parini, "Mutual coupling in a finite planar array of rectangular apertures", Electronics Letters 23(21), pp. 1169 - 1170, February 1987.

[11] O. Werther, R. Minihold, "LTE System Specifications and their Impact on RF & Base Band Circuits", Rhode & Schwarz Application Note, 1MA221_1E, April 2013.

[12] Z. Wang, A. C. Bovik, H. R. Sheikh, and E. P. Simoncelli, "Image Quality Assessment: From Error Visibility to Structural Similarity," IEEE Transactions on Image Processing, Volume 13, Issue 4, pp. 600- 612, 2004.